Chapter 5
Germanene, Stanene and Other 2D Materials

Germanene and stanene (also sometimes written stannene or called tinene) are 2D materials composed of germanium and tin atoms respectively arranged in a honeycomb structure similarly to graphene and silicene. The atomic structure of freestanding germanene and stanene is buckled like in the case of silicene (see Fig. 2.4). DFT calculations (Kresse and Joubert 1999) performed by projector augmented wave (PAW) method (Blöchl 1994) and adopting PBE functional (Perdew et al. 1996) result in a lattice constants 4.06 and 4.67 Å and buckling heights of 0.69 and 0.85 Å for germanene and stanene respectively. The structure of germanene was first theoretically proposed together with that of silicene (Takeda and Shiraishi 1994) while stanene was explored later (Cahangirov et al. 2009; Sahin et al. 2009; Xu et al. 2013).

The vibrational modes of germanene and stanene are much softer than those of silicene and graphene. In fact, the maximum of the longitudinal optical (LO) mode is 183, 286, 555 and 1605 cm^{-1} for stanene, germanene, silicene and graphene, respectively. Some studies have found imaginary frequencies in the out-of-plane acoustic (ZO) modes of germanene and stanene near the Brillouin zone center (Cahangirov et al. 2009; Sahin et al. 2009; Tang et al. 2014). However, these imaginary frequencies indicating instability are just artifacts caused by the numerical accuracy that is not enough to evaluate the modes of germanene and stanene that are too soft. One way to get rid of them is to use a finer mesh grid in the DFT calculation. The phonon modes of germanene and stanene resulting from this kind of calculation are presented in Fig. 5.1. Here, one can see the similarities between the modes of germanene and stanene with those of silicene, shown in Fig. 2.5.

The fact that all phonon modes are positive indicate the stability of germanene and stanene. However, the larger ionic radius of germanium and tin atoms make them even more in favor of sp^3 hybridization compared to silicon. This is mirrored in the bond angles of germanene and stanene that are θ=112.4° and 111.4° which can

S. Cahangirov et al., *Introduction to the Physics of Silicene and other 2D Materials*, Lecture Notes in Physics 930,
DOI 10.1007/978-3-319-46572-2_5

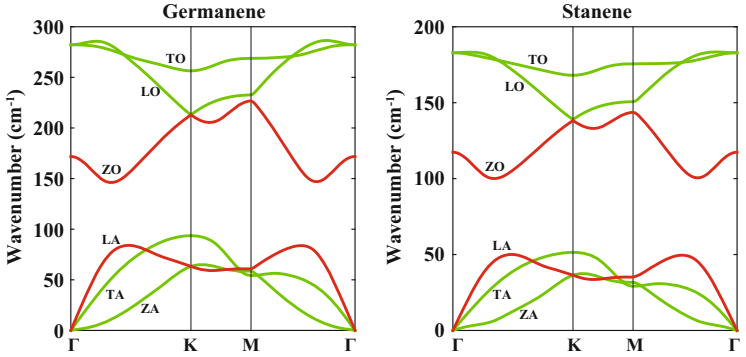

Fig. 5.1 The phonon modes of buckled germanene and stanene. The out of plane, transverse and longitudinal acoustic and optical modes are denoted by ZA, TA, LA, ZO, TO and LO, respectively. The LA and ZO modes of germanene and stanene (shown by *red lines*) change significantly upon transformation from a planar (not shown here) to the buckled structure. A similar change is observed in silicene as shown in Fig. 2.5

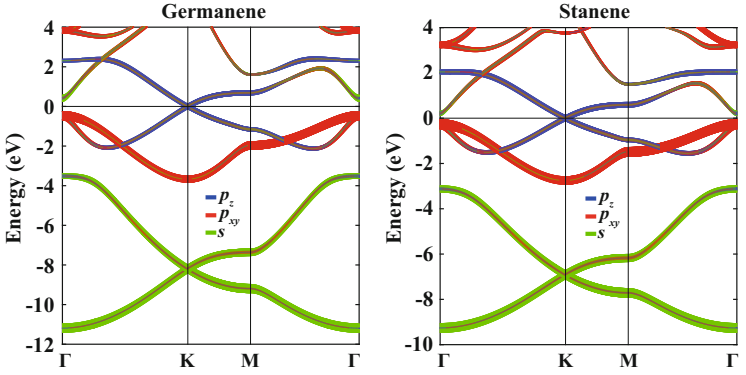

Fig. 5.2 The electronic structures of buckled germanene and stanene. The orbital character of each state is shown by *colors*. The width of each line is proportional to the contribution from the orbital denoted by the *color* of that line. The orbital with lower contribution is plotted on top of the one that has higher contribution, which makes all contributions visible

be translated into the hybridization sp^D through $D = -1/cos(\theta)$ yielding 2.63 and 2.74, respectively. The corresponding value for silicene is 2.27, as shown in Chap. 2. This means that the 2D structure of germanene and stanene are even more delicate and vulnerable to forming 3D structures by clustering. However, stabilization of germanene and stanene could be possible on certain substrates as it is the case for silicene.

The electronic energy bands of germanene and stanene are presented in Fig. 5.2. The linearly crossing bands are preserved both in buckled germanene and stanene.

The contribution from s and p_{xy} states to these bands is enhanced due to higher buckling compared to silicene. The Fermi velocity was calculated (using PAW-PBE) to be 0.52×10^6 m/s for germanene which is almost equal to that of silicene (see Chap. 2) while for stanene it is 0.47×10^6 m/s. The most dramatic change, compared to silicene, happens near the Brillouin zone center (Γ-point) where the gap shrinks from 3.13 eV for silicene to 0.88 and 0.48 eV for germanene and stanene, respectively. This gap shrinks even further, down to zero, when stanene is fluorinated. However, it opens back if spin-orbit coupling is included in the calculation (Xu et al. 2013). This results in an intriguing electronic structure discussed below.

The exotic electronic properties of silicene, like being a topological insulator, are further pronounced in germanene and stanene due to an even larger spin-orbit coupling in germanium and tin atoms compared to silicon. Including spin-orbit coupling opens a 1.55, 23.9 and 73.5 meV gap between the linearly crossing bands of silicene, germanene and stanene (Liu et al. 2011a,b). This is already enough to observe the quantum spin Hall effect at temperatures much higher than that of the liquid nitrogen. Remarkably, it is possible to go even further by functionalizing stanene (Xu et al. 2013). Fluorinating stanene saturates its π-orbitals opening a 2 eV band gap at the K-point. However, it also closes the gap at the Γ-point, if spin-orbit is not included. Including spin-orbit coupling induces a 0.3 eV gap making fluorinated stanene a large-gap quantum spin Hall insulator that can operate at room temperature. Similar to the well known case of HgTe quantum wells (Bernevig et al. 2006; König et al. 2007), the electronic states of fluorinated stanene become topologically nontrivial through s-p type band inversion at the Γ-point (Xu et al. 2013). No such inversion occurs in hydrogenated stanene, also called stanane. Accordingly, the nanoribbons of stanene and fluorinated stanene have helical edge states linearly crossing at the Fermi level while stanane nanoribbons don't have such states (Xu et al. 2013).

Another way to functionalize stanene is to pattern it with the dumbbell structures (Tang et al. 2014). Similar to the silicene case (see Chap. 2) the most energetically favorable structure is large honeycomb dumbbell stanene (LHDT). The LHDT structure is 0.18 eV/atom more favorable than buckled stanene. The band structure calculation including spin-orbit coupling results in a 40 meV non-trivial gap at the Γ-point of LDHT. In this case, the spin-orbit coupling lifts the degeneracy of two p_{xy} states at the valence band edge and the band inversion occurs between the p_z state at the conduction band edge and one of the p_{xy} states. Similar to the case of fluorinated stanene, zigzag nanoribbons of LDHT were shown to have helical edge states.

Very recently, both germanene and stanene were synthesized on substrates. Germanene was synthesized on Au(111) substrates by molecular beam epitaxy (Dávila et al. 2014). In this respect, synthesis of germanene is very similar to that of silicene (Vogt et al. 2012), only here silver sample was exchanged for a gold (111) one and the silicon source was replaced by a germanium evaporator to deposit Ge atoms onto a clean Au(111) surface prepared in a standard fashion by Ar+ ion bombardment and annealing. Low energy electron diffraction (LEED) and STM observations were performed at room temperature (RT) at different stages of the growth, carried out at several substrate temperatures to determine potential candidates for germanene in an overall multiphase diagram, as was already the case for silicon deposition onto Ag(111). Germanene phases were obtained at 200 °C growth temperature at about 1 mL coverage, as estimated from the 32 % attenuation of the Au $4f_{7/2}$ core level intensity. It covers extended regions, larger than 50×50 nm^2 in size, with a honeycomb appearance and a very small corrugation of just 0.01 nm, as well as with a weak long range modulation in STM imaging, as displayed in Fig. 5.3. Core-level spectroscopy revealed that Ge 3d states can be fitted with a very narrow, asymmetric single component essentially signaling a unique environment of the germanium atoms at the surface while spots corresponding to $\sqrt{7} \times \sqrt{7}$, $\sqrt{19} \times \sqrt{19}$ and 5×5 superstructure of Au(111) were observed in the LEED pattern. STM image also supports a $\sqrt{7} \times \sqrt{7}$ superstructure.

Actually, it is possible to place Ge atoms on top of the Au(111) surface in such a way that each of them feels the same environment. This arrangement is shown in Fig. 5.3d. It turns out that this particular configuration corresponds to $\sqrt{3} \times \sqrt{3}$ germanene matched by $\sqrt{7} \times \sqrt{7}$ Au(111). This explains the $\sqrt{7} \times \sqrt{7}$ superstructure observed in the LEED and the STM measurements. Furthermore, this matching is made possible by stretching germanene layer which would make it rather flat. This is also in accordance with STM findings. DFT calculations starting from such a configuration results in optimized structures that reproduces the experimental STM profile (Dávila et al. 2014).

Even more uniform phase of germanene was synthesized at only 80 °C on the Al(111) surface (Derivaz et al. 2015). In this case, 2×2 supercell of germanene is matched by 3×3 supercell of the Al(111) surface. Stanene, on the other hand, was synthesized on Bi_2Te_3(111) substrate (Zhu et al. 2015). Due to the lattice match stanene has no reconstruction. STM and ARPES measurements have confirmed the atomic and electronic structures of stanene on Bi_2Te_3(111) obtained by DFT calculations.

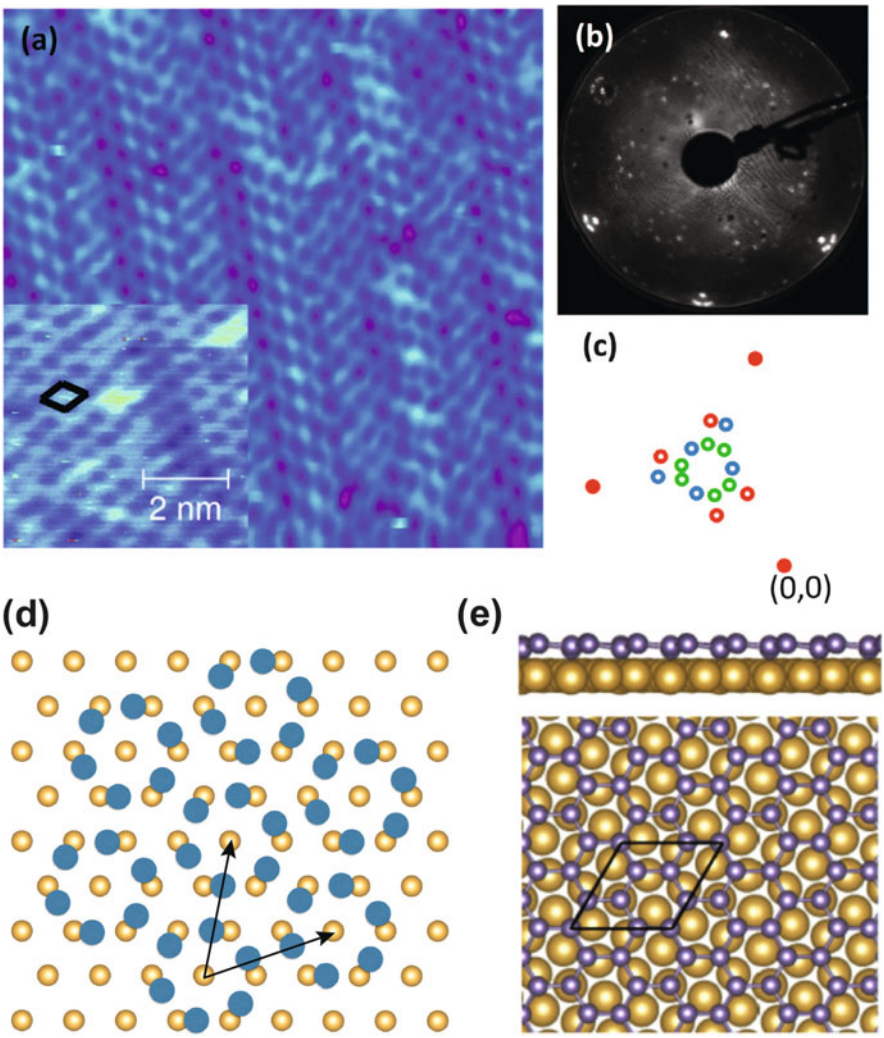

Fig. 5.3 (**a**) 16.2 nm×16.2 nm STM image of the modulated honeycomb $\sqrt{7} \times \sqrt{7}$ superstructure with a close-up in the *bottom left corner* (sample bias: 1.12 V, 1.58 nA; the $\sqrt{7} \times \sqrt{7}$ unit cell is drawn in *black*); (**b**) associated LEED pattern taken at 59 V; (**c**) schematic illustration of one sixth of the pattern, *filled dots*: hidden (0,0) spot and integer order spots, *open circles*: spots corresponding to the $\sqrt{7} \times \sqrt{7}$ superstructure (in *red*), the $\sqrt{19} \times \sqrt{19}$ one (in *green*) and the 5×5 (in *blue*). (**d**) Initial position of Ge atoms (*blue*) on the top layer of Au(111) (*gold*). In this configuration, each Ge atom has the same environment. The *arrows* correspond to both $\sqrt{3} \times \sqrt{3}$ supercell of germanene and $\sqrt{7} \times \sqrt{7}$ supercell of Au(111) surface. (**e**) Top and side view of atomic structure after optimization. Adapted from Dávila et al. (2014)

5.1 Binary Compounds of Group IV and Group III–V Elements

The elemental 2D materials like silicene, germanene and stanene are natural extensions of graphene. One can extend the search for novel 2D materials further by taking inspiration from hexagonal boron nitride (BN) that has been studied in detail (Rubio et al. 1994; Jin et al. 2009). This approach leads to consideration of the binary compounds of Group IV elements like SiC, GeSn and etc. and those of Group III–V elements like GaAs, BP and others (Sahin et al. 2009).

In Fig. 5.4 we present a general trend for the energy per unit cell versus the lattice constant. Some structures like graphene and hexagonal boron nitride have only one

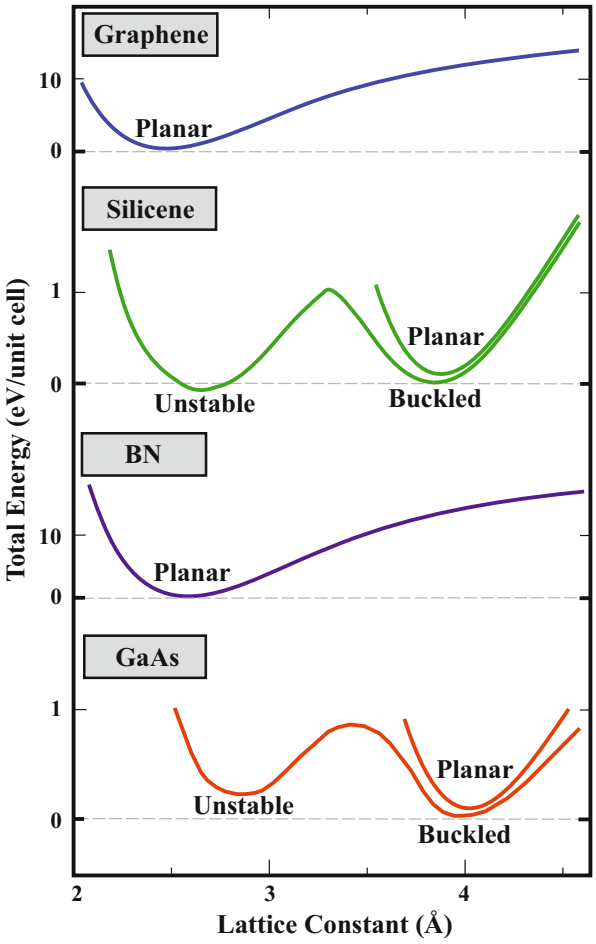

Fig. 5.4 Comparison of the total energy per unit cell versus the lattice constant for graphene, silicene, hexagonal BN sheet and GaAs sheet. For each structure, zero of energy is set to the minimum energy of a stable configuration. Adapted from Sahin et al. (2009)

energy minimum corresponding to a planar geometry while others like silicene and GaAs have three energy minima. However, only the slightly buckled structure that has a lattice constant close to that of the planar structure is stable. The other two minima correspond to unstable structures. In fact, by analysing all possible binary compounds of Group IV and Group III–V, it was shown that structures having at least one element from the first row (that is B, C or N) have stable planar minimum while others are buckled (Sahin et al. 2009).

Phonon dispersions of 2D binary compounds of Group IV elements are presented in Fig. 5.5. The longitudinal and transverse optical modes are separated from other modes. This separation is larger when the constituting elements are further apart in the periodic table. In planar structures, the out-of-plane optical mode mixes with acoustical modes while in the buckled structures this mode is in between acoustical and other optical modes. Note that, all modes are positive for any combination of Group IV elements, which means that they are all stable.

In Fig. 5.6, we present the phonon dispersions of stable 2D materials constituted by Group III–V elements. One can immediately notice the similarity between the phonon dispersions of graphene, germanene and stanene with that of the Group III–V compounds at the same row, namely, BN, GaAs and InSb. Interestingly, 2D AlP

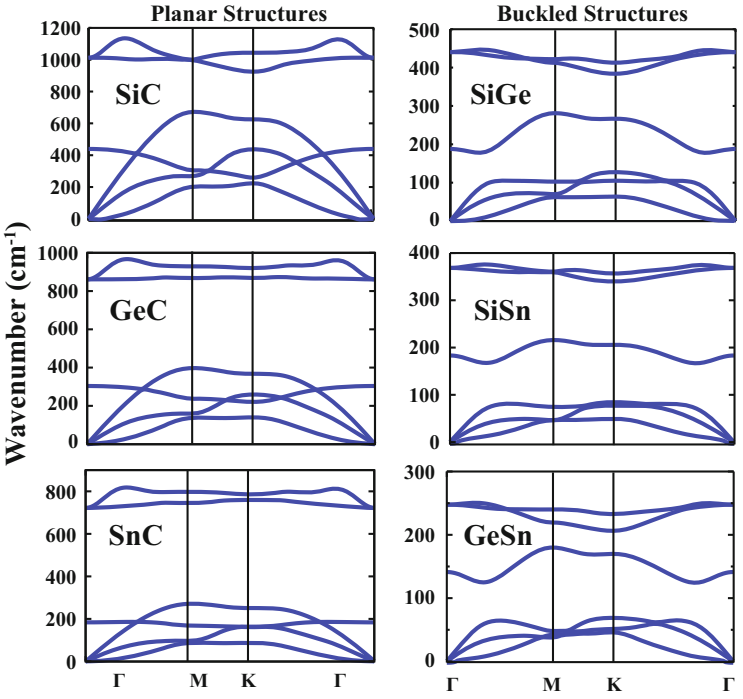

Fig. 5.5 Phonon dispersions of planar and buckled structures of 2D materials constituted by two different Group IV elements. Adapted from Sahin et al. (2009)

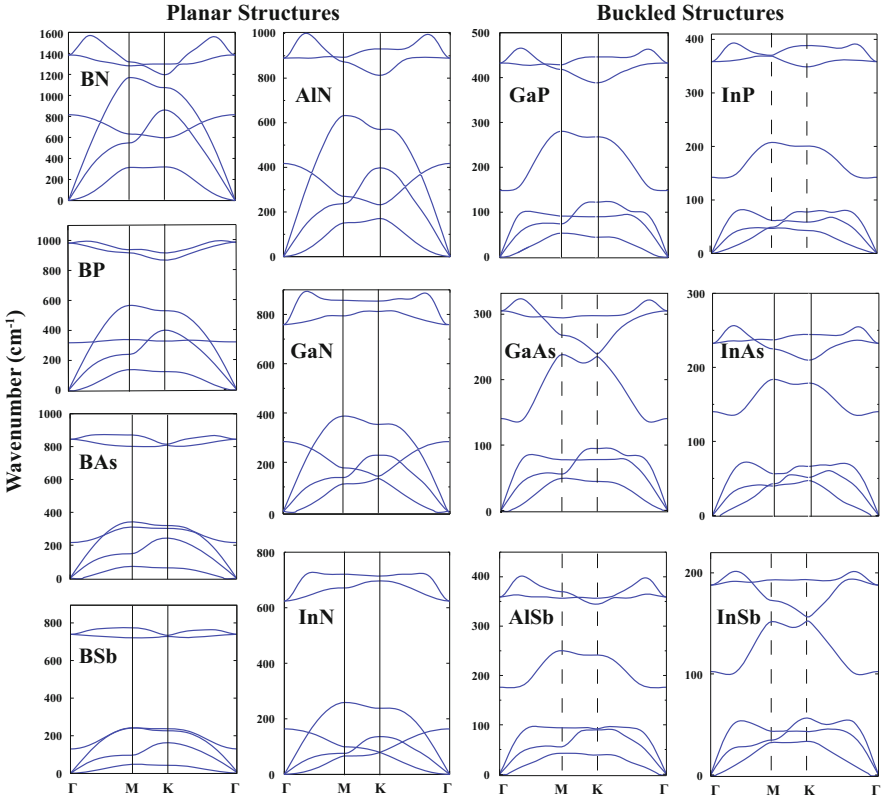

Fig. 5.6 Phonon dispersions of planar and buckled structures of 2D materials constituted by Group III–V elements. Adapted from Sahin et al. (2009)

that is constituted by elements from the silicon row is unstable, all other combination of elements in the neighbourhood of Al and P are stable. This exception needs further elaboration. The out of plane optical mode comes very close to the other optical modes at the K point of GaAs and InSb structures that are formed from the same row elements. BN is also formed by the same row elements but it is planar and thus has an out-of-plane optical mode that is mixed with acoustical modes, similar to aforementioned planar structures.

There are several clear trends in properties of 2D materials composed of Group IV and Group III–V elements. In Fig. 5.7 we present the lattice constant and the in-plane stiffness versus the cohesive energy per atomic pair. Note that, planar and buckled structures are clearly separated from each other while sharing the same linear dependence on the cohesive energy versus lattice constant plot. In-plane stiffnesses of graphene and hexagonal BN are significantly higher than that of the rest. Here the cohesive energy, E_c, is calculated using the expression $E_c = E_T[AB] - E_T[A] - E_T[B]$, where $E_T[AB]$ is the total energy per A-B pair of

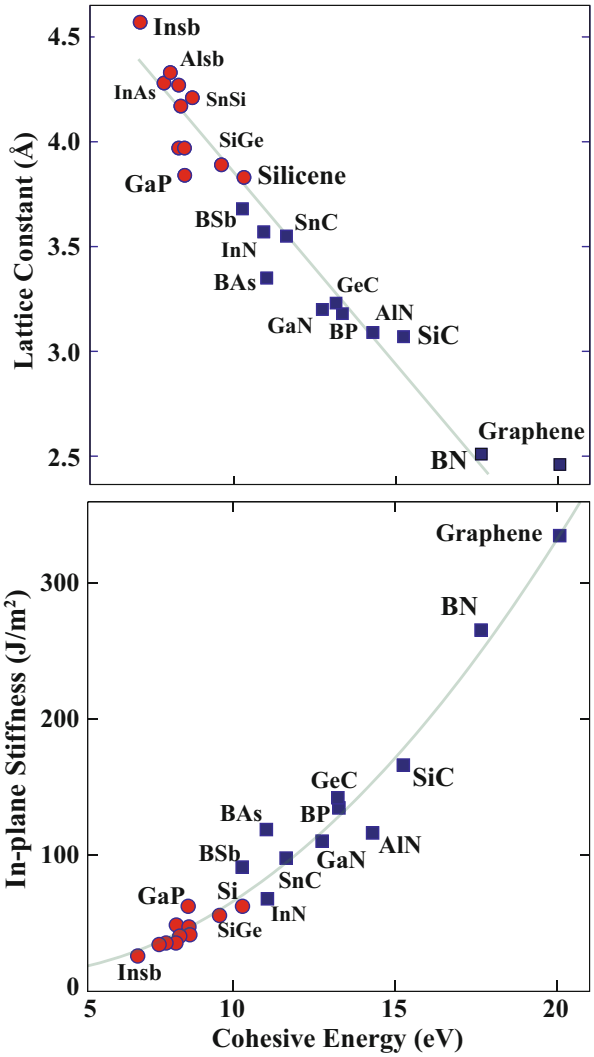

Fig. 5.7 Cohesive energy versus lattice constant and in-plane stiffness versus cohesive energy trends for 2D materials constituted by Group IV and Group III–V elements. Planar and buckled structures are denoted by *purple squares* and *red circles*, respectively. Adapted from Sahin et al. (2009)

the optimized honeycomb structure while $E_T[A]$ and $E_T[B]$ are the total energies of free A and B atoms corresponding to nonmagnetic state. In-plane stiffness is calculated by focusing on the harmonic range of the elastic deformation, where the structure responds to strain ϵ linearly. The rectangular supercell is pulled in x- and y-directions over a regular mesh of strains ϵ_x and ϵ_y while the strain energy, $E_S = E_T(\epsilon) - E_T(\epsilon = 0)$ is determined. The data is then fitted to a two-dimensional

quadratic polynomial expressed by

$$E_S(\epsilon_x, \epsilon_y) = a_1\epsilon_x^2 + a_2\epsilon_y^2 + a_3\epsilon_x\epsilon_y \tag{5.1}$$

where ϵ_x and ϵ_y are the small strains along x- and y-directions in the harmonic region. Due to the isotropy of the honeycomb structure $a_1 = a_2$. These parameters can be related to the elastic stiffness constants by $a_1 = a_2 = (h \cdot A_0/2) \cdot C_{11}$, $a_3 = (h \cdot A_0) \cdot C_{12}$, where h and A_0 are the effective thickness and equilibrium unitcell area of the system, respectively. Hence one obtains Poisson's ratio $\nu = -\epsilon_{trans}/\epsilon_{axial}$, which is equal to $C_{12}/C_{11} = a_3/2a_1$. Similarly, the in-plane stiffness, $C = h \cdot C_{11} \cdot (1 - (C_{11}/C_{12})^2) = (2a_1\text{-}(a_3)^2/2a_1)/(A_0)$. The calculated value of the in-plane stiffness of graphene is in agreement with the experimental value of 340 (N/m) (Lee et al. 2008).

Band structures of these materials were also investigated both by LDA and G_0W_0 methods. Interested reader is referred to Sahin et al. (2009).

5.2 Borophene and Phosphorene

Isolated hexagonal boron sheet is theoretically predicted to be unstable (Boustani et al. 1999). Boron has been shown to have metallic layered structure composed of buckled triangular motifs in a partially filled honeycomb structure at a specific hole density (Boustani et al. 1999; Tang and Ismail-Beigi 2007). This configuration allows the kind of chemical bonds that boron forms best: bonds among three atoms rather than between two. However, as for silicene, germenene and stanane, a hexagonal boron layer could be stabilized by the interaction with a substrate. Indeed crystalline 2D boron sheets (i.e., borophene) on silver surfaces have been recently synthesized (Mannix et al. 2015).

Phosphorene is a 2D material derived from the layered allotrope of phosphorus called "black phosphorus". Black phosphorus is the most stable allotrope of phosphorus and was synthesized a century ago (Bridgman 1914). It has black color, as the name suggests, and in general is very similar to graphite in terms of both appearance and atomic structure. Despite this similarity, the single layer of black phosphorus, named phosphorene, was unexplored, even for a decade after the synthesis of graphene, the single layer of graphite. Phosphorene became a center of attention after two groups managed to exfoliate single and few layers of phosphorene from black phosphorus (Reich 2014; Liu et al. 2014; Li et al. 2014). The field-effect transistor made from few layers of phosphorene was shown to reach the charge carrier mobility of $1000\,\mathrm{cm^2\,V^{-1}\,s^{-1}}$ (Liu et al. 2014).

The atomic structures of black phosphorus and phosphorene are presented in Fig. 5.8. The structural parameters of the freestanding phosphorene shown in the right panel of Fig. 5.8 are obtained by DFT calculations using the PAW-PBE approach (Kresse and Joubert 1999; Blöchl 1994; Perdew et al. 1996). The thickness of phosphorene which is the height difference between the top and the bottom

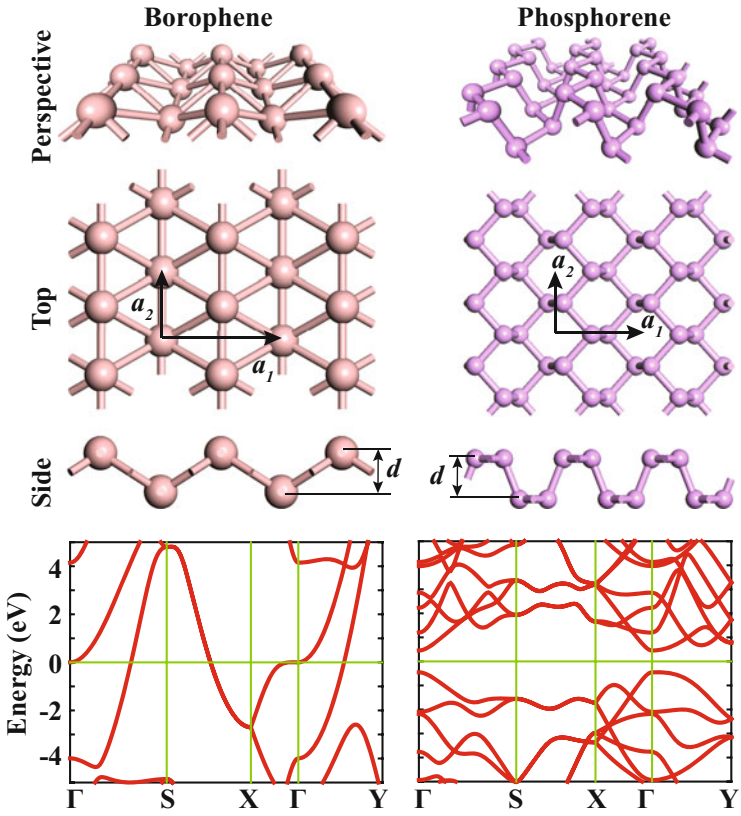

Fig. 5.8 Atomic and electronic structure of borophene and phosphorene

phosphorus atoms is 2.10 Å. Although the threefold coordination of atoms in phosphorene reminds the honeycomb structure of silicene, there are significant differences. The structure of phosphorene is reminiscent of the (110) plane of the diamond structure while silicene is related to the (111) plane. However, the bond angles of phosphorene are significantly smaller than the tetrahedral angle 109.5° due to the fact that phosphorus is a group V element.

Experiments have shown that black phosphorus has a direct band gap of 0.31–0.36 eV at the Γ-point (Warschauer 1963; Narita et al. 1983; Maruyama et al. 1981) which is very well reproduced by the DFT calculations (Liu et al. 2014). The DFT calculations also show that, as one goes from bulk black phosphorus to single layer phosphorene, the band gap increases linearly with respect to the inverse of the number of phosphorene layers reaching 1.0 eV at the single layer. The band gap of phosphorene becomes 2.31 eV (Çakır et al. 2014) when the self-energy corrections are included at the G_0W_0 level (Hedin 1965; Shishkin and Kresse 2007). On the other hand, the excitonic binding energy calculated by solving the

Bethe-Salpeter equation (Salpeter and Bethe 1951; Onida et al. 2002) was found to be 0.70 eV (Çakır et al. 2014). Hence, the optical gap is predicted to be 1.61 eV. This is in agreement with the measured photoluminescence spectrum of single layer phosphorene that has a peak at 1.45 eV (Liu et al. 2014).

The atomic structure of phosphorene is highly anisotropic compared to other 2D materials that have honeycomb symmetry. This anisotropy is reflected in the optical absorption spectra of phosphorene (Tran et al. 2014). Monolayer phosphorene absorbs light polarized along the armchair direction (a_1 in Fig. 5.8) with energies 1.1 eV and above. This lower bound in the energy of absorbed armchair-polarized light goes down to 300 meV when the number of layers are increased from monolayer phosphorene to the bulk black phosphorus. On the other hand, light polarized along the zigzag direction (a_2 in Fig. 5.8) is absorbed if its energy exceeds 2.5 eV. In this case, the absorption spectrum has minor changes when the number of layers are varied. This means that armchair-polarized light having energy in the range from 1.1 to 2.5 eV will be absorbed by phosphorene while zigzag-polarized light with the same energy will pass through. This makes phosphorene a natural linear polarizer with an energy window that can be tuned by the number of layers.

5.3 Transition Metal Dichalcogenides

The remarkable properties of monolayer graphene have triggered interest in ultra-thin materials with similar crystal structure. Among these, Transition Metal Dichalcogenides (TMDs) are the most promising. Here we note that especially this field is evolving very fast and we can only mention a few points. Bulk forms of TMDs have been used in industrial applications such as lubricant materials, coating technology, water splitting and petroleum refining. Although there were many studies before, the research on TMDs got an extra boost after the synthesis of graphene.

Although TMDs in bulk form have been investigated for long time, recent advances in experimental techniques revealed many unique properties of single layers of TMDs:

- while graphene is semimetallic, single layer TMDS are semiconductors,
- TMDs become much more resistant against mechanical deformations when they are synthesized in the form of a single layer,
- the band gaps of TMDs strongly depend on the number of layers,
- even the direct/indirect nature of the allowed optical transitions can be controlled via the number of layers,
- TMDs exhibit strain-tunable vibrational spectra and electronic properties,
- in contrast to graphene, the surfaces of TMDs possess tunable chemical properties,
- TMDs have localized plasmons with a confinement factor that can be an order of magnitude larger than that of graphene

- chiral light emission from K and K' valleys is possible in TMDs
- for different combinations of metal and chalcogen atoms TMDs can form various phases that have diverse electronic properties ranging from semiconducting, superconducting to ferromagnetic.

Because of these reasons TMDs are very promising materials for nanoscale electronic and opto-electronic device applications.

TMDs are a class of materials with the general formula MX_2, where M is a transition metal element and X is a chalcogen (S, Se or Te). In each individual layer of their lamellar crystal structure, a monolayer lattice of metal atoms is sandwiched between two chalcogen layers, and, hence, each metal atom is surrounded by six chalcogen atoms. While weak layer-layer interactions in TMDs enable easy exfoliation of individual layers, strong covalent nature of in-plane bonds makes these structures strong and flexible. As shown in Fig. 5.9, depending on their constituent atoms, the TMDs' crystal structures can be found in three different phases; H, T and distorted-T. In the following we survey these phases in details.

Many of the TMDs such as MoS_2, $MoSe_2$, $MoTe_2$, WS_2 and WSe_2 crystallize in a hexagonal graphene-like structure. As shown in Figs. 5.9a and 5.10a, each metal atom binds six chalcogen atoms by forming a prismatic configuration. This trigonal prismatic configuration has D_{3h} lattice symmetry. Because of large atomic distances between metal atoms the interaction of d-orbital states are negligible. So far, experiments have revealed that single layers of dichalcogenides of molybdenum and tungsten have ground state structures with D_{3h} symmetry. This phase of single layer TMDs is called 1H. In bulk structures, stacking of individual layers results in an alternatingly rotated sequence which is called hexagonal symmetric 2H phase that belongs to the inversion-symmetric D_{6h} point group (see Fig. 5.10b). In contrast to weak inter-layer interactions that allows easy mechanical exfoliation, metal and chalcogen atoms have strong intra-plane bonds that have covalent character.

Another unique characteristic of the TMDs' H phase is thickness dependent electronic properties. Starting from the early experiments (Mak et al. 2010; Splendiani et al. 2010) revealing the strongly enhanced photoluminescence intensity of ultrathin MoS_2, the thickness dependent characteristics of this family has been the focus

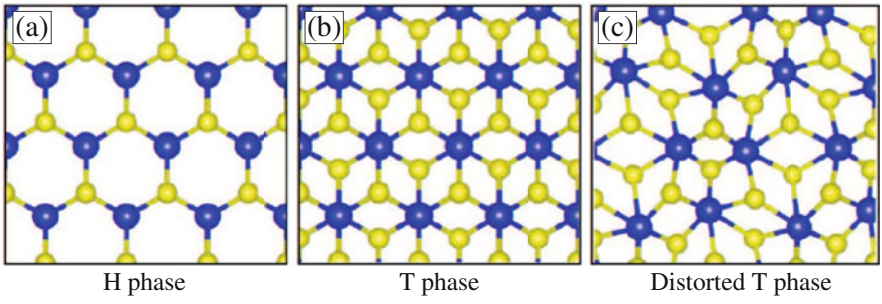

Fig. 5.9 Possible phases of TMD crystal structures are visualized from a top view of their single layers

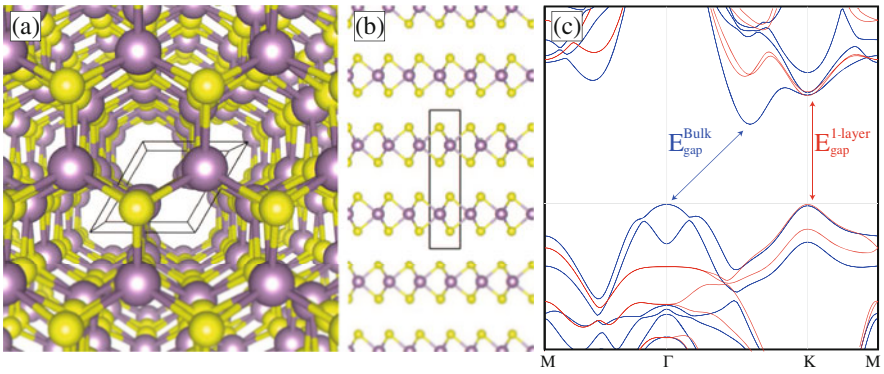

Fig. 5.10 (**a**) Perspective top view and (**b**) side view of MX2s in H phase. The primitive unit cell containing two layers is represented by the *black rectangle*. (**c**) Characteristic band dispersions of H-MX2 type bulk (in *blue*) and single layer (in *red*) structures

of interest. The main reason of such a dramatic change in the optical spectrum stems from band gap crossover. The characteristic electronic band dispersion of dichalcogenides of Mo and W is presented in Fig. 5.10c. It is seen that the bulk structure is an indirect band gap semiconductor with band edges located at the Γ and $\Gamma - K$ points, while the monolayer crystal structure is a semiconductor with a direct band gap at the K high symmetry point. While the top of the valence band is mainly composed of Mo-d orbitals, the conduction band minimum is formed by hybridization of Mo-*d* and Se-*p* orbitals. Another interesting point in the electronic dispersion is the large spin-orbit splitting which is always found around the K symmetry point. Such a large spin-orbit splitting has never been reported for other graphene-like materials.

Furthermore, the 1H phase is not the only possible phase for single layer TMDs. Some of the single layer TMDs such as TaS_2, $TiSe_2$, SnS_2 and HfS_2 form trigonal anti-prismatic configurations as shown in Fig. 5.9b. Differing from the H phase, bulk structures with T phase prefer AA type stacking in which same type of atoms are located on top of each other. However, the trigonal anti-prismatic configuration of monolayer T structure belongs to the D_{3d} point group. Although, 1H and 1T configurations result in slightly different hexagonal crystal structures, their electronic spectrum turns out to be very different. Most of the experimental data and theoretical predictions show that 1T structures have metallic character (Ozaydin et al. 2014, 2015; Joe et al. 2014; Kang et al. 2015). One notes that the spatial overlap of the d-state electrons with neighboring metal and chalcogen atoms plays a more important role in the T phase.

In contrast to TMDs in the H phase, TMDs forming T phase have robust metallic behavior which is independent from their thickness. In addition, recent studies have also revealed that apart from TMDs some other dihalogen and dichalcogen compounds may form stable monolayer structures that have 1T symmetry. For

instance, while $FeCl_2$ is a ferromagnetic semiconductor with half-metallic behavior (Torun et al. 2015) SnS_2 is a direct bandgap semiconductor (Ahn et al. 2015).

More interestingly, recent studies have also revealed that single layer TMDs may form distorted lattice structures. For instance, it was noticed that mechanically exfoliated ReS_2 and $ReSe_2$ single layers, which are expect to be in the 1T phase, are neither in the 1H nor the 1T phase (Tongay et al. 2014; Yang et al. 2015). As firstly demonstrated for ReS_2, 1H and 1T phases can only be obtained through simple total energy calculations, but, however, they are dynamically unstable. Since each Re atom has seven valence electrons, there is one dangling electron on each Re atom when the six-coordinated H or T phase is formed. However, when the distorted-T phase is constructed through the formation of Re-Re dimers the total energy of the system is 1.1 eV (per ReS_2 unit) lowered and the resulting structure was found to be dynamically stable as well.

Due to the increased Re-Re interaction in ReS_2 the hexagonal lattice is narrowed along one of the lattice vectors and the symmetry of the structure obeys neither D_{3d} nor D_{3h} symmetry. This disturbed lattice structure with its broken symmetry is referred as distorted-1T structure (see Fig. 5.9c). Here the phase transition is directly driven by the Re atoms. It appears that the use of different metal atoms during the synthesis of MX_2 structures may result in new TMDs that have various phases and novel electronic properties. Formation of such dimers was also confirmed by HRTEM measurements (Tongay et al. 2014). Moreover, such a reconstruction also leads to a decrease in intraplanar polarization and to a vanishing interlayer coupling. As a result of these combined unusual effects the ReS_2 and $ReSe_2$ crystal structures become electronically and vibrationally decoupled. As presented in Fig. 5.11d, as a consequence of Re-induced inter planar decoupling, the eigenfrequencies of the Raman-active vibrational modes of ReS_2 change very slightly even under very high hydrostatic pressures. However, mode hardening in the phonon frequencies of MoS_2 is much larger than in ReS_2.

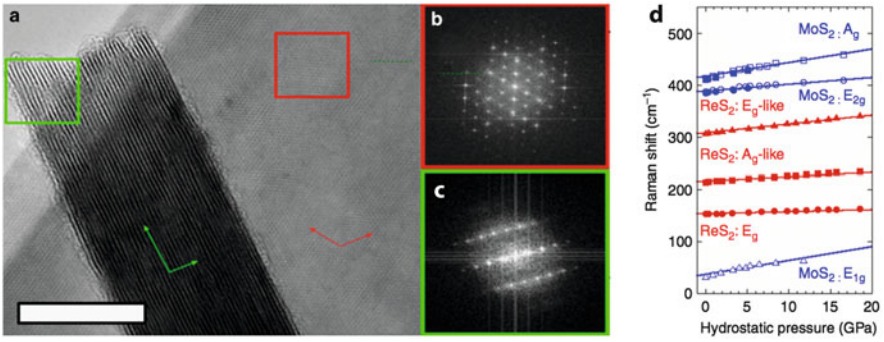

Fig. 5.11 (**a**) HRTEM images of ReS_2 taken from in- and out-of-plane directions; scale bar: 20 nm. (**b**) The flake's basal plane is perpendicular to the electron beam and (**c**) the other basal plane of the flake is oriented parallel to the beam. (**d**) Pressure dependent shift in Raman-active phonon modes of ReS_2 and MoS_2

More interestingly, recent studies also revealed that distorted phases of TMDs can also be induced by simple adsorption processes. Although the T phase of MoS_2 has never been experimentally observed, it is possible to stabilize a T phase over the H phase through adsorption of Li atoms on the MoS_2 surface (Esfahani et al. 2015). Moreover, the dynamical stability of the resulting 1T-Li_2MoS_2 structure was investigated by performing phonon and molecular dynamics calculations at finite temperatures. They showed that the perfect T structure is unstable toward clustering of Mo and Li atoms even at low temperatures, while the distorted structure remains stable up to about 500 K. Therefore, as supported by phonon calculations, fully lithium covered MoS_2, Li_2MoS_2, has a distorted 1T structure that resembles the diamond-like dimerized crystal structure of ReX_2 (X=S, Se).

5.4 Chalcogenides of Sn

Very recent experiments have also shown that apart from the elemental monolayer crystal structure of tin, called stanene, various tin sulphide structures can be stabilized in ultra-thin single layer form.

Similar to TMDs MoS_2 and WS_2 monolayer SnS_2 possesses a three-atomic hexagonal primitive unit cell. However, differing from TMDs that have mostly a 1H phase, SnS_2 crystallizes in a 1T phase. As shown in Fig. 5.12, the trigonally arranged subplane of Sn atoms is sandwiched by two S-subplanes. While the 1H phase belongs to the $P\bar{6}m2$ space group where subplanes are *ABA* stacked, the 1T phase is a member of the $P\bar{3}m2$ space group where subplanes are *ABC* stacked. Recently, Bacaksiz et al. found that the 1T phase of the SnS_2 is 875 meV/cell more favorable over the 1H phase, by performing ab initio DFT calculations. The primitive lattice vectors of 1T-SnS_2 can be given as $\mathbf{v}_1 = a(\frac{1}{2}, \frac{\sqrt{3}}{2}, 0)$, $\mathbf{v}_2 = a(\frac{1}{2}, -\frac{\sqrt{3}}{2}, 0)$ where $|\mathbf{v}_1| = |\mathbf{v}_2|$ and a is the lattice constant ($a = b$). In this cell the fractional coordinates of Sn, top S and bottom S atoms are given by $(\frac{|v_1|}{2}, \frac{|v_1|}{2}, 0)$, $(\frac{|v_1|}{6}, \frac{|v_1|}{6}, \frac{c}{2})$, and $(\frac{5|v_1|}{6}, \frac{5|v_1|}{6}, -\frac{c}{2})$, respectively (where c is the distance between the subplanes of S atoms). In this configuration the lattice parameter and Sn-S inter-atomic distance are calculated to be 2.59 and 3.68 Å, respectively.

While TMDs such as MoS_2 and WS_2 are direct band gap semiconductors whose valence band and conduction band edges are located at the K symmetry point, the 1T-SnS_2 crystal is a semiconductor with an indirect bandgap of 1.58 eV. The HSE06 corrected bandgap is found to be 2.40 eV. It was also shown that 1T-SnS_2 has a nonmagnetic ground state. In addition, a possibility of easy tuning of the stacking sequence of SnS_2 bilayers by two different ways, charging and application of loading pressure, was described.

Very recently, Ahn et al. reported the successful synthesis of monolayer SnS_2 on SiO_2/Si substrates by a vapor transport method (Ahn et al. 2015). In the growth procedure while the precursor molecules are SnO_2 and S_2, the products are determined by the added H_2. It was also measured that SnS_2 exhibits *n*-type

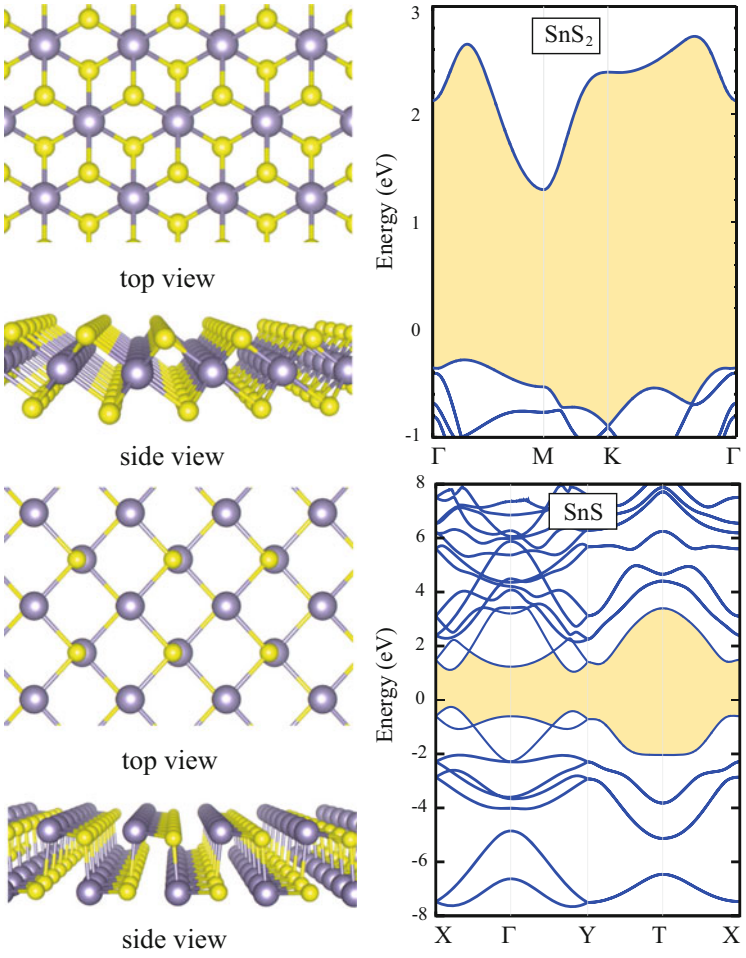

Fig. 5.12 Atomic structure and electronic band dispersion of SnS_2 (*top*) and SnS (*bottom*)

electronic character with a 2.77 eV band gap, which implies presence of defects or impurities at its surface of SnS_2. The interest on monolayer orthorhombic crystals was triggered by the synthesis of phosphorene that has easy tunable and highly anisotropic electronic properties. In their study, Ahn et al. also achieved the synthesis of orthorhombic SnS crystals by tuning the amount of H_2 added during gas-phase synthesis.

Experiments also revealed that *n*-type doping occurs in synthesized orthorhombic SnS which has an energy band gap of 1.26 eV. As shown in Fig. 5.12, differing from hexagonal 1T phase of SnS_2, the orthorhombic phase possesses a direct band gap at the vicinity of the zone center which makes it more suitable for optoelectronic device applications.

5.5 Portlandite and Brucite

The synthesis of monolayer graphene from bulk graphite not only gave researchers, for the first time, access to a quasi-two dimensional (2D) crystal, but it also drew significant attention to similar layered bulk structures such as Alkaline Earth Metal Hydroxides (AEMHs). AEMHs can be represented by the general chemical formula $M(OH)_2$ where M is the alkaline-earth metal. Bulk single crystals of AEMHs are layered structures that belong to the P3m1 space group. In this layered crystal structure shown in Fig. 5.13 the metal atoms fill all of the octahedral sites in alternating layers, while the OH pairs form a hexagonal close packed arrangement. In AEMHs, while the bonding has mainly ionic character, it has also partial covalent character.

One of the most well-known AEMH is portlandite, presented by the chemical formula $Ca(OH)_2$, which is the main product of hydration of portland cement. Although portlandite has been known for a long time, synthesis and understanding the characteristic properties of its monolayer structures have not been studied until 2015. In our study we, experimentally and theoretically investigated bulk, bilayer, and monolayer portlandites (Aierken et al. 2015). Firstly we showed that single crystal $Ca(OH)_2$ monolayers can be exfoliated from their bulk form onto different substrates. By performing ab initio total energy calculations, the lattice parameter, the Ca-O distance and the O-H distance are calculated as 3.62, 2.38 and 0.97 Å, respectively. The electronic band dispersion shown in Fig. 5.14a shows that single layer portlandite is a direct semiconductor with a large bandgap. While GGA-PBE approximated bandgap is 3.67 eV, HSE06 approach gives bandgap of 5.16 eV which is usually close to the optical bandgap of the materials.

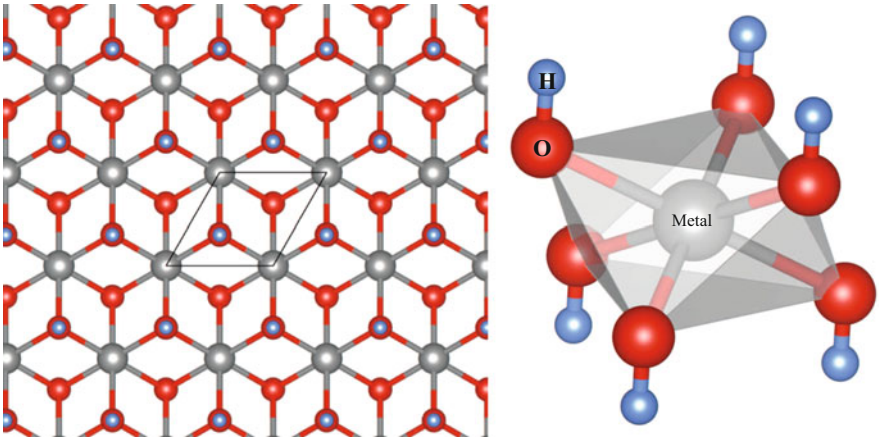

Fig. 5.13 *Top and tilted side view* of $M(OH)_2$. The primitive unitcell is shown by the *black lozenge*. The six-coordinated bonding nature of the metal atom is shown by polyhedra. *Grey*, *red* and *blue balls* represent metal atom, oxygen and hydrogen, respectively

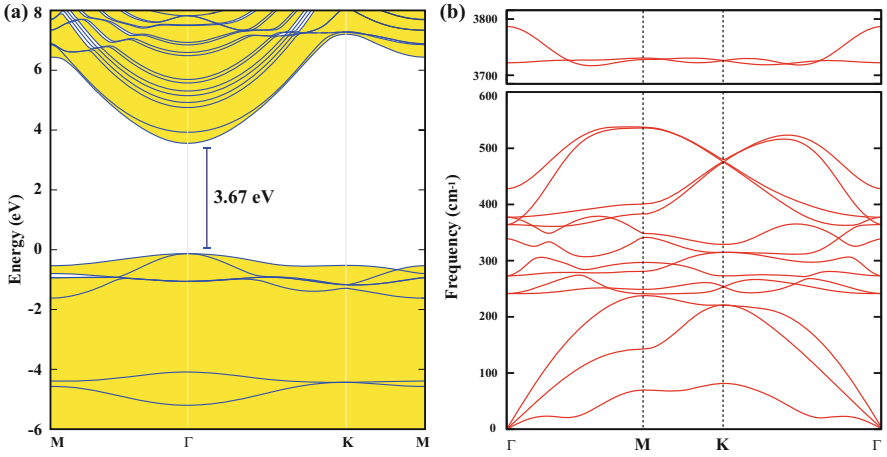

Fig. 5.14 (**a**) Electronic band dispersion and (**b**) vibrational spectrum of single layer $Ca(OH)_2$

Analysis of the phonon dispersion of the monolayer structure revealed that it is a dynamically stable crystal structure and the decomposition of the vibration representation of optical modes at the zone center is $\Gamma = 4E_u + 2A_{2u} + 4E_g + 2A_{1g}$. As shown in the right panel of Fig. 5.14b, there are four Raman-active phonon branches around 240, 350, 390, and 3700–3800 cm^{-1}. It is also worth noting that as opposed to other TMDCs structures that have the 1T phase, the presence of H atoms results in the existence of two different E_g and A_{1g} modes. It was also found that, similar to the Raman shift measurements observed from the bulk crystal structure, the monolayer material also has high-frequency OH stretching modes at 3700–3800 cm^{-1}.

Another well-known AEMH is brucite, with the chemical formula $Mg(OH)_2$. The bulk brucite mineral has been used widely in industrial applications as magnesium source and flame retardant. Our experimental measurements and calculations revealed that single layer crystal structures of AEMHs of Ca and Mg share many of the same electronic and vibrational characteristics (Fig. 5.15). While bulk brucite has a direct bandgap of 6.17 eV at the Γ point, (HSE06 corrected bandgap), the direct bandgap of monolayer brucite is calculated to be 4.80 eV. Regarding the indirect-to-direct bandgap crossover in well-known TMDs, AEMHs that have a robust, thickness-independent band character, have an entirely different behavior. Moreover, our experiments demonstrated that when MoS_2 is supported by $Mg(OH)_2$, its photoluminescence intensity is enhanced significantly. It is seen that due to the structural stability, thickness-independent robust electronic behavior, good dielectric property and unique optical performance in heterostructure applications AEMHs hold promise for future nanoscale device applications.

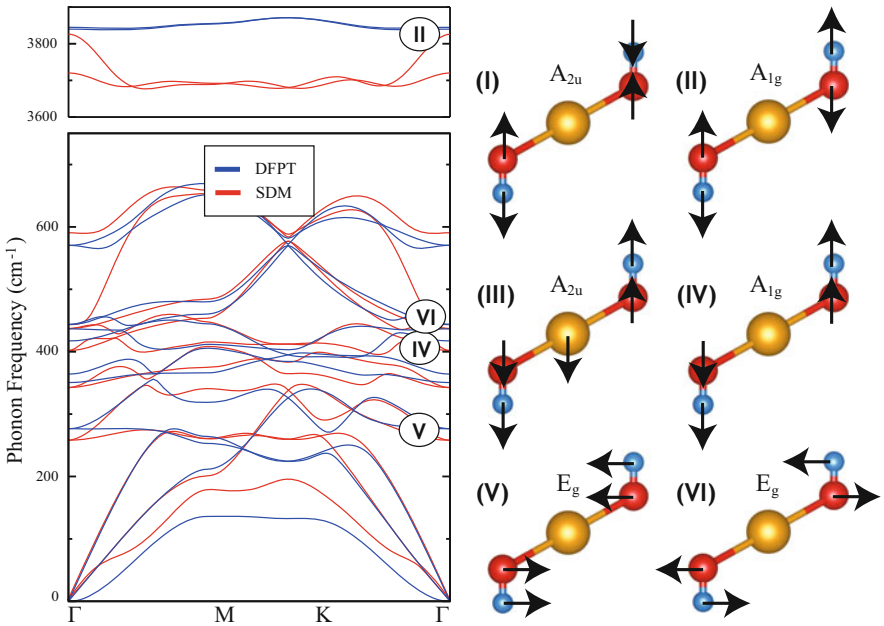

Fig. 5.15 *Left panel*: phonon dispersion of monolayer brucite calculated by using two different methodologies. *Right panel*: characteristic eigenmotions. *Orange*, *red* and *blue balls* represent Mg, O and H atoms, respectively

5.6 Concluding Remarks

Layered materials offer a new perspective in the development of low dimensional materials with a wealth of novel electronic and mechanical properties. An exciting aspect of 2D materials is stacking them into structures that are still very thin, such that we take advantage of the vastly different properties of different layered materials, creating previously unimagined devices made of atomically thick components. Each 2D material known or to be discovered is like a Lego brick that we can use to build new materials with tailored properties.

We have been living with those layered materials for very long time: graphite, hex-BN, the family of transition metal dichalgogenides (TMD), layered oxides, etc. All of them are well characterized in a bulk 3D stacked configuration, however the boom of the field of 2D materials started with the rise of graphene and its derivatives. Exfoliation of already existing bulk materials offer a direct way to get layered single (and few layers) of hex-BN and TMDs. The impressive rise of graphene, due to its exceptional electronic and mechanical properties, has spurred many scientists to searching for alternative 2D materials with heavy elements such as Si, Ge and Sn. This race has led to the synthesis and/or prediction of many other atomically-thin materials. These materials promise to improve nano electronics and open up entirely new ways of carrying information, for example by exploiting

quantum properties such as the electron spin ("spintronics"), or the presence of two electron's valley states in many 2D materials that offers a direct way to digital switches ("valleytronics"). Since no net flow of charge is required in spintronics or valleytronics the problem of heating and power dissipation might disappear.

In the last years we have witnessed an important incorporation in that family of layered material based on new single element layered structures made of group III (B), group IV (Si,Ge and Sn) and group V (P) elements have been proposed and few of them already synthesized not in isolated form but supported on metallic substrates. Particularly the 2D group IV materials that include graphene, silicene, germanene and stanene and group V phosphorene have attracted enormous interests due to their exotic electronic properties and potential applications in nanoelectronics, spintronics, optical materials as well as an ideal testbed for the understanding of novel phenomena as topological superconductivity, near-room-temperature quantum ("half-integer") anomalous Hall (QAH) effect enhanced thermoelectric performance and dissipationless electric conduction at room temperature. The QSHE is of broad interest because of its scientific importance as a novel quantum state of matter and its potential for technological applications in the fields of spintronics, valleytronics and quantum computation.

As the material research community turns its attention to 2D materials beyond graphene, new 2D materials are discovered (or re-discovered) on a weekly basis. There are estimated to be a few hundred more that are waiting to be explored, and the research on 2D materials will stay active in the foreseeable future. Among the vast number of 2D materials, elemental 2D materials occupies a special place due to their diverse properties and their mono-elemental nature. It's conceivable that eventually only few 2D materials will find their way into industry, if at all. We believe that elemental 2D materials will be among those selected few.

References

Ahn, J.H., Lee, M.J., Heo, H., Sung, J.H., Kim, K., Hwang, H., Jo, M.H.: Deterministic two-dimensional polymorphism growth of hexagonal n-type SnS_2 and orthorhombic p-type SnS crystals. Nano Lett. **15**, 3703–3708 (2015)

Aierken, Y., Sahin, H., Iyikanat, F., Horzum, S., Suslu, A., Chen, B., Senger, R.T., Tongay, S., Peeters, F.M.: Portlandite crystal: bulk, bilayer, and monolayer structures. Phys. Rev. B **91**, 245413 (2015)

Bernevig, B.A., Hughes, T.L., Zhang, S.C.: Quantum spin hall effect and topological phase transition in HgTe quantum wells. Science **314**, 1757–1761 (2006)

Blöchl, P.E.: Projector augmented-wave method. Phys. Rev. B **50**, 17953–17979 (1994)

Boustani, I., Quandt, A., Hernndez, E., Rubio, A.: New boron based nanostructured materials. J. Chem. Phys. **110** (1999)

Bridgman, P.W.: Two new modifications of phosphorus. J. Am. Chem. Soc. **36**, 1344–1363 (1914)

Cahangirov, S., Topsakal, M., Aktürk, E., Şahin, H., Ciraci, S.: Two- and one-dimensional honeycomb structures of silicon and germanium. Phys. Rev. Lett. **102**, 236804 (2009)

Çakır, D., Sahin, H., Peeters, F.M.: Tuning of the electronic and optical properties of single-layer black phosphorus by strain. Phys. Rev. B **90**, 205421 (2014)

Dávila, M.E., Xian, L., Cahangirov, S., Rubio, A., Le Lay, G.: Germanene: a novel two-dimensional germanium allotrope akin to graphene and silicene. New J. Phys. **16**, 095002 (2014)

Derivaz, M., Dentel, D., Stephan, R., Hanf, M.C., Mehdaoui, A., Sonnet, P., Pirri, C.: Continuous germanene layer on Al(111). Nano Lett. **15**, 2510–2516 (2015)

Esfahani, D.N., Leenaerts, O., Sahin, H., Partoens, B., Peeters, F.M.: Structural transitions in monolayer MoS_2 by lithium adsorption. J. Phys. Chem. C **119**, 10602–10609 (2015)

Hedin, L.: New method for calculating the one-particle Green's function with application to the electron-gas problem. Phys. Rev. **139**, A796–A823 (1965)

Jin, C., Lin, F., Suenaga, K., Iijima, S.: Fabrication of a freestanding boron nitride single layer and its defect assignments. Phys. Rev. Lett. **102**, 195505 (2009)

Joe, Y.I., Chen, X.M., Ghaemi, P., Finkelstein, K.D., de la Pena, G.A., Gan, Y., Lee, J.C.T., Yuan, S., Geck, J., MacDougall, G.J., Chiang, T.C., Cooper, S.L., Fradkin, E., Abbamonte, P.: Emergence of charge density wave domain walls above the superconducting dome in 1T-$TiSe_2$. Nat. Phys. **10**, 421–425 (2014)

Kang, J., Sahin, H., Peeters, F.M.: Mechanical properties of monolayer sulphides: a comparative study between MoS_2, HfS_2 and TiS_3. Phys. Chem. Chem. Phys. **17**, 27742–27749 (2015)

König, M., Wiedmann, S., Brüne, C., Roth, A., Buhmann, H., Molenkamp, L.W., Qi, X.L., Zhang, S.C.: Quantum spin Hall insulator state in HgTe quantum wells. Science **318**, 766–770 (2007)

Kresse, G., Joubert, D.: From ultrasoft pseudopotentials to the projector augmented-wave method. Phys. Rev. B **59**, 1758–1775 (1999)

Lee, C., Wei, X., Kysar, J.W., Hone, J.: Measurement of the elastic properties and intrinsic strength of monolayer graphene. Science **321**, 385–388 (2008)

Li, L., Yu, Y., Ye, G.J., Ge, Q., Ou, X., Wu, H., Feng, D., Chen, X.H., Zhang, Y.: Black phosphorus field-effect transistors. Nat. Nanotechnol. **9**, 372–377 (2014)

Liu, C.C., Feng, W., Yao, Y.: Quantum spin Hall effect in silicene and two-dimensional germanium. Phys. Rev. Lett. **107**, 076802 (2011a)

Liu, C.C., Jiang, H., Yao, Y.: Low-energy effective hamiltonian involving spin-orbit coupling in silicene and two-dimensional germanium and tin. Phys. Rev. B **84**, 195430 (2011b)

Liu, H., Neal, A.T., Zhu, Z., Luo, Z., Xu, X., Tom´anek, D., Ye, P.D.: Phosphorene: an unexplored 2d semiconductor with a high hole mobility. ACS Nano **8**, 4033–4041 (2014)

Mak, K.F., Lee, C., Hone, J., Shan, J., Heinz, T.F.: Atomically thin mos_2: a new direct-gap semiconductor. Phys. Rev. Lett. **105**, 136805 (2010)

Mannix, A.J., Zhou, X.F., Kiraly, B., Wood, J.D., Alducin, D., Myers, B.D., Liu, X., Fisher, B.L., Santiago, U., Guest, J.R., Yacaman, M.J., Ponce, A., Oganov, A.R., Hersam, M.C., Guisinger, N.P.: Synthesis of borophenes: anisotropic, two-dimensional boron polymorphs. Science **350**, 1513–1516 (2015)

Maruyama, Y., Suzuki, S., Kobayashi, K., Tanuma, S.: Synthesis and some properties of black phosphorus single crystals. Physica **105B**, 99–102 (1981)

Narita, S., Akahama, Y., Tsukiyama, Y., Muro, K., Mori, S., Endo, S., Taniguchi, M., Seki, M., Suga, S., Mikuni, A., Kanzaki, H.: Electrical and optical properties of black phosphorus single crystals. Physica **117B–118B**, 422–424 (1983)

Onida, G., Reining, L., Rubio, A.: Electronic excitations: density-functional versus many-body Green's-function approaches. Rev. Mod. Phys. **74**, 601–659 (2002)

Ozaydin, H.D., Sahin, H., Senger, R.T., Peeters, F.M.: Formation and diffusion characteristics of Pt clusters on graphene, 1H-MoS_2 and 1T-TaS_2. Ann. Phys. **526**, 423–429 (2014)

Ozaydin, H.D., Sahin, H., Kang, J., Peeters, F.M., Senger, R.T.: Electronic and magnetic properties of 1 T-$TiSe_2$ nanoribbons. 2D Mater. **2**, 044002 (2015)

Perdew, J.P., Burke, K., Ernzerhof, M.: Generalized gradient approximation made simple. Phys. Rev. Lett. **77**, 3865–3868 (1996)

Reich, E.S.: Phosphorene excites materials scientists. Nature **506**, 19 (2014)

Rubio, A., Corkill, J.L., Cohen, M.L.: Theory of graphitic boron nitride nanotubes. Phys. Rev. B **49**, 5081–5084 (1994)

Sahin, H., Cahangirov, S., Topsakal, M., Bekaroglu, E., Aktürk, E., Senger, R.T., Ciraci, S.: Monolayer honeycomb structures of group-IV elements and III-V binary compounds: first-principles calculations. Phys. Rev. B **80**, 155453 (2009)

Salpeter, E.E., Bethe, H.A.: A relativistic equation for bound-state problems. Phys. Rev. **84**, 1232–1242 (1951)

Shishkin, M., Kresse, G.: Self-consistent GW calculations for semiconductors and insulators. Phys. Rev. B **75**, 235102 (2007)

Splendiani, A., Sun, L., Zhang, Y., Li, T., Kim, J., Chim, C.Y., Galli, G., Wang, F.: Emerging photoluminescence in monolayer mos2. Nano Lett. **10**, 1271–1275 (2010)

Takeda, K., Shiraishi, K.: Theoretical possibility of stage corrugation in Si and Ge analogs of graphite. Phys. Rev. B **50**, 14916–14922 (1994)

Tang, H., Ismail-Beigi, S.: Novel precursors for boron nanotubes: The competition of two-center and three-center bonding in boron sheets. Phys. Rev. Lett. **99**, 115501 (2007)

Tang, P., Chen, P., Cao, W., Huang, H., Cahangirov, S., Xian, L., Xu, Y., Zhang, S.C., Duan, W., Rubio, A.: Stable two-dimensional dumbbell stanene: a quantum spin Hall insulator. Phys. Rev. B **90**, 121408 (2014)

Tongay, S., Sahin, H., Ko, C., Luce, A., Fan, W., Liu, K., Zhou, J., Huang, Y.S., Ho, C.H., Yan, J., Ogletree, D.F., Aloni, S., Ji, J., Li, S., Li, J., Peeters, F.M., Wu, J.: Monolayer behaviour in bulk ReS2 due to electronic and vibrational decoupling. Nat. Commun. **5** (2014). doi:10.1038/ncomms4252

Torun, E., Sahin, H., Singh, S.K., Peeters, F.M.: Stable half-metallic monolayers of $FeCl_2$. Appl. Phys. Lett. **106**, 192404 (2015)

Tran, V., Soklaski, R., Liang, Y., Yang, L.: Layer-controlled band gap and aniso-tropic excitons in few-layer black phosphorus. Phys. Rev. B **89**, 235319 (2014)

Vogt, P., De Padova, P., Quaresima, C., Avila, J., Frantzeskakis, E., Asensio, M.C., Resta, A., Ealet, B., Le Lay, G.: Silicene: compelling experimental evidence for graphene like two-dimensional silicon. Phys. Rev. Lett. **108**, 155501 (2012)

Warschauer, D.: Electrical and optical properties of crystalline black phosphorus. J. Appl. Phys. **34**, 1853–1860 (1963)

Xu, Y., Yan, B., Zhang, H.J., Wang, J., Xu, G., Tang, P., Duan, W., Zhang, S.C.: Large-gap quantum spin Hall insulators in tin films. Phys. Rev. Lett. **111**, 136804 (2013)

Yang, S., Wang, C., Sahin, H., Chen, H., Li, Y., Li, S.S., Suslu, A., Peeters, F.M., Liu, Q., Li, J., Tongay, S.: Tuning the optical, magnetic, and electrical properties of $ReSe_2$ by nanoscale strain engineering. Nano Lett. **15**, 1660–1666 (2015)

Zhu, F.F., Chen, W.J., Xu, Y., Gao, C.L., Guan, D.D., Liu, C.H., Qian, D., Zhang, S.C., Jia, J.F.: Epitaxial growth of two-dimensional stanene. Nat. Mater. **14**, 1020–1025 (2015)